Icarus 231 (2014) 122–130

Contents lists available at ScienceDirect

Icarus

journal homepage: www.elsevier.com/locate/icarus

The role of snowfall in forming the seasonal ice caps of Mars: Models and constraints from the Mars Climate Sounder

Paul O. Hayne [a,*], David A. Paige [b], Nicholas G. Heavens [c], the Mars Climate Sounder Science Team

[a] NASA – Jet Propulsion Laboratory, California Institute of Technology, Pasadena, CA, United States
[b] Department of Earth and Space Sciences, University of California, Los Angeles, CA, United States
[c] Department of Atmospheric and Planetary Sciences, Hampton University, Hampton, VA, United States

ARTICLE INFO

Article history:
Received 4 April 2013
Revised 5 September 2013
Accepted 18 October 2013
Available online 8 December 2013

Keywords:
Mars
Mars, polar caps
Mars, atmosphere
Mars, climate
Atmospheres, structure

ABSTRACT

Wintertime observations of the martian polar regions by orbiting spacecraft have provided evidence for carbon dioxide clouds, which measurably alter the polar energy budget and the annual CO_2 cycle. However, it has remained unclear whether snowfall contributes a substantial quantity to the accumulating seasonal ice caps. We develop models to constrain precipitation rates based on observations of south polar CO_2 clouds by the Mars Climate Sounder (MCS), and show that snowfall contributes between 3% and 20% by mass to the seasonal deposits at latitudes 70–90°S. The lower bound on this estimate depends on a minimum effective cloud particle size of ~50 μm, derived by comparing the short lifetimes (less than a few hours) of some clouds with calculated sedimentation velocities. Separate constraints from infrared spectra measured by MCS suggest CO_2 cloud particles in the size range 10–100 μm. Snow particles are not likely to re-sublime before reaching the surface, because the lower atmosphere in this region remains near saturation with respect to CO_2. Based on cooling rate calculations, snowfall originating below 4 km altitude likely contributes a comparable or greater amount to the seasonal deposits than the rest of the atmosphere. Due to the positive feedback between cloud particle number density and radiative cooling, CO_2 snow clouds should propagate until they become limited by the availability of condensation nuclei or CO_2 gas. Over the south polar residual cap, where cloud activity is greatest, atmospheric radiative cooling rates are high enough to offset heat advected into the polar regions and maintain consistent snowfall. At latitudes of 60–80°S the lower atmosphere tends to be slightly sub-saturated and rapid cooling by mechanical lift driven by orography or convergent flow may be required to initiate a snowstorm, consistent with the more sporadic clouds observed by MCS in this region, and their correlation with topographic features. Snowfall and accumulation at the surface are found to be inevitable consequences of the polar energy budget, unless advection redistributes heat from lower latitudes in much greater quantities than expected.

1. Introduction

On the basis of theory (Gierasch and Goody, 1968) and direct observations (Ivanov and Muhleman, 2001; Colaprete et al., 2003; Hayne et al., 2012), previous studies have suggested the common occurrence of carbon dioxide snowfall in the martian polar winter. Radiative and dynamical cooling rates predicted by GCMs suggest atmospheric precipitation could account for ~25–40% of the mass of solid CO_2 forming the seasonal polar cap (Pollack et al., 1990; Forget et al., 1998; Kuroda et al., 2013). Heat transport into the polar regions from lower latitudes is not likely to be sufficient to offset this atmospheric energy deficit in the absence of solar heating during the long polar night (Paige and Ingersoll, 1985). Topography-driven atmospheric waves may generate highly heterogeneous, but repeatable snowfall patterns (Colaprete et al., 2008). Microphysical models indicate that once on the surface, CO_2 ice grains would undergo rapid sintering, eliminating particles smaller than 1 mm on time scales of days (Clark et al., 1983; Eluszkiewicz, 1993; Eluszkiewicz et al., 2005), consistent with the shortest observed time scale for the disappearance of regions of low infrared brightness temperature ("cold spots") under a clear atmosphere (Hansen, 1999; Titus et al., 2001). Therefore, small-grained deposits observed to persist over longer periods must be resupplied by frequent snowfall (Hayne et al., 2012).

Near-infrared laser echoes from optically thick polar night clouds (Neumann et al., 2003) indicate cloud particles are larger than ~1 μm, and detailed CO_2 ice nucleation and growth models consistently predict particle radii in the range ~10–100 μm (Wood, 1999; Colaprete and Toon, 2002; Colaprete et al., 2008). Fall times

* Corresponding author.
E-mail addresses: Paul.O.Hayne@jpl.nasa.gov, phayne@gps.caltech.edu (P.O. Hayne).

0019-1035/$ - see front matter © 2013 Elsevier Inc. All rights reserved.
http://dx.doi.org/10.1016/j.icarus.2013.10.020

for particles in this size range originating from one scale height (∼7 km) above the surface are on the order of a few hours (see Section 5.1). Furthermore, polar winter temperature profiles typically remain near the saturation profile below ∼30 km (Kleinböhl and et al., 2009; Hu et al., 2012), such that falling grains are more likely to grow than re-sublimate on their descent to the surface. In fact, a temperature profile remaining near saturation should occur if atmospheric cooling is buffered by the latent heat of deposition of snow particles (Wood, 1999), so the observed correspondence can be seen as evidence for this buffering mechanism. Considerations similar to those above have led previous investigators to conclude that optically thick clouds in the martian polar winter are probably precipitating, and attention has turned to quantifying snowfall rates and cloud formation processes (Forget et al., 1998; Colaprete et al., 2003, 2005, 2008).

In this paper, we investigate the phenomenon of carbon dioxide snowfall with models constrained by infrared observations by the Mars Climate Sounder (MCS). Opacity profiles derived from the MCS observations allow us to model the radiative cooling of the cloudy south polar winter atmosphere, placing constraints on precipitation rates (Section 3). These rates can be compared to those resulting from adiabatic cooling in the form of orographic precipitation, the subject of Section 4. In Section 5, we develop models for the sedimentation of CO_2 snow particles comprising the south polar clouds observed by MCS, from which we estimate precipitation rates through time as the cloud falls to the surface. Finally, we synthesize these results to quantify the role of snowfall in forming the martian seasonal ice caps, and discuss the remaining uncertainties.

2. Instrumentation and dataset

The Mars Climate Sounder (MCS) is a multi-spectral visible and infrared filter radiometer onboard the Mars Reconnaissance Orbiter (MRO), which began its science phase in November of 2006. One of the primary goals motivating the design of the MCS investigation was probing the energy balance of the polar regions (McCleese et al., 2007). The instrument has nine channels spanning the wavelength range ∼0.3–45 μm (33,000–220 cm^{-1}), with one visible and eight IR channels. An important capability of MCS is independent two-axis scanning, which allows the telescopes to view either the limb (typically forward in the orbit track), or nadir. Each spectral channel consists of a linear array of 21 thermopile detectors, each with a field of view (FOV) of ∼3.6 × 6.1 mrad, corresponding to a typical vertical limb resolution of ∼4 km, and a surface resolution of ∼1 km (smeared by spacecraft motion to ∼6 km). In the limb sounding mode, the detectors' shorter dimension is oriented vertically, with the 21 detectors spanning limb tangent points from the surface up to ∼100 km altitude. Variable infrared emission by warm surfaces can affect aerosol retrievals within about 4 km of the surface, due to radiance in the FOV wings, but this effect is relatively small in the cold polar regions considered here.

In this paper, we focus on a subset of CO_2 cloud opacity retrievals obtained for the south polar winter from MCS limb measurements during Mars Year 29 (as defined by Clancy et al. (2000)). These profiles have tangent points within 20° of the pole, and were acquired near midnight on June 24, 2008 UTC, when the areocentric longitude of the Sun (L_s, defined such that northern vernal equinox occurs at 0°) was 89.5°, just prior to the winter solstice (Fig. 1). Optically thick clouds also occur in the northern hemisphere winter, but here we focus on the southern hemisphere due to the greater availability of retrieved atmospheric profiles. The temperature retrieval algorithm is described by Kleinböhl and et al. (2009) and the CO_2 ice opacity retrieval is described by Hayne et al. (2012), who derived constraints on the size of particles composing the CO_2 clouds based on spectral features in the observed limb radiance profiles. Here we also interpret the time-variability of cloud opacity recorded by MCS as an important constraint on particle size, as discussed in Section 5.

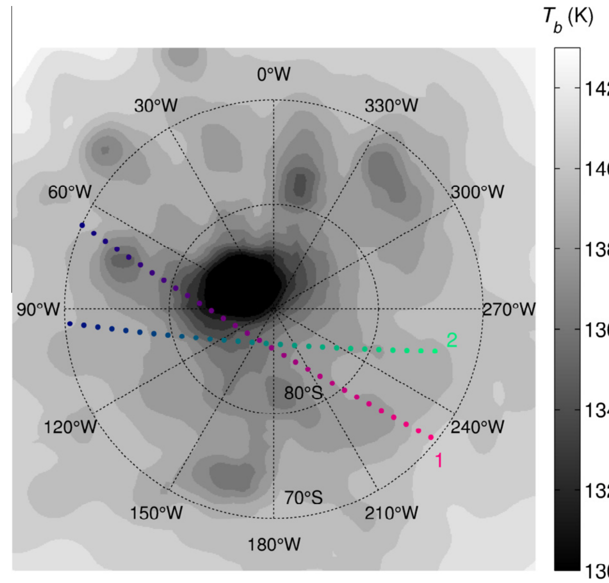

Fig. 1. South polar winter surface brightness temperatures at 32 μm retrieved from MCS data (grayscale), with locations of profiles used in this study indicated by the colored dots. Each of the two MRO orbits occurred on June 24, 2008 UTC.

3. Cooling rates constrained by MCS observations

During the polar night, an isolated atmospheric column cools by infrared emission to space until carbon dioxide begins to condense, at which point release of latent heat buffers the temperature against further cooling. Neglecting conductive heat exchange with the ground, the atmospheric heat balance during this period can be represented by

$$L\frac{dm}{dt} = F_{IR} - Q_{Horz}, \tag{1}$$

where $L \approx 5.9 \times 10^5$ J kg^{-1} is the latent heat of sublimation of CO_2, dm/dt (kg m^{-2} s^{-1}) is the rate of formation of CO_2 ice particles, Q_{Horz} is the heating rate due to horizontal advection of sensible heat, and F_{IR} is the net outgoing infrared flux at the boundaries of the atmosphere. Precipitation rates dm/dt can then be estimated from column-integrated infrared fluxes, offset by the net heat advection from outside the polar night. At a given level in a plane-parallel atmosphere, the radiative cooling rate is related to the flux divergence by

$$\left[\frac{dT}{dt}\right]_{IR} = -\frac{1}{\rho c_p}\frac{dF}{dz}, \tag{2}$$

where ρ and c_p are the local density and heat capacity of the atmosphere, z is the vertical coordinate, and the net infrared flux at a given height is

$$F(z) = F^{\uparrow}(z) - F^{\downarrow}(z). \tag{3}$$

In the analysis that follows, infrared cooling rates were calculated for a cloudy atmosphere using the techniques described in Appendix A. Adiabatic cooling due vertical motion is an important process at scales of the surface topography and will be addressed in a separate subsection below.

Clouds promote cooling by increasing the effective infrared emissivity of the atmosphere, because the CO_2 gas is essentially transparent outside the strong 15 μm bending fundamental, whereas solid CO_2 particles are not. Cooling due to infrared emission by aerosols can be quantified using MCS radiance measurements. We calculated infrared cooling rates for the gas and aerosol based on retrieved south polar winter temperature and CO_2 cloud opacity profiles (Fig. 2). Where the cloud opacity retrievals were unreliable due to large line-of-sight optical depths or missing data, we use an extrapolation to the surface assuming particles are well mixed in the lower atmosphere. We performed retrievals and calculated cooling rates for three different CO_2 ice particle sizes (10, 30 and 100 μm) and surface emissivities 1.0 and 0.7, as well as a cloud containing both CO_2 ice and water ice. The resulting flux divergence profiles in Fig. 3 shows that the entire atmospheric column experiences net infrared cooling, as expected during polar night. Due to their larger infrared absorption cross sections than CO_2 ice, water ice and dust particles enhance atmospheric cooling, though it is difficult to quantify these minor constituents within the cloudy polar night using MCS spectra alone. In the lowermost atmosphere, where CO_2 ice retrievals are most uncertain, infrared cooling is dominated by the gaseous thermal emission.

Column-integrated infrared fluxes presented in Fig. 4 and Table 1 show infrared cooling alone can result in significant amounts of atmospheric condensation within the observed cloudy region. The total rate of outgoing long wave radiation from the surface-atmosphere column during this period is

$$F_{net} = \bar{\varepsilon}\sigma T_s^4 \approx 15\text{–}25\ \mathrm{W\ m^{-2}}, \tag{4}$$

where $\bar{\varepsilon} \approx 0.6\text{–}1.0$ is the effective emissivity (Forget et al., 1998) and $T_s \approx 145$ K is the surface temperature. Converted to a deposition rate, the range is $F_{net}/L \approx 25\text{–}42\ \mathrm{mg\ m^{-2}\ s^{-1}}$. Based on the results shown in Table 1, carbon dioxide precipitation during the observation period could account for ~3–20% of the total surface-plus-atmosphere deposition rate. This range accounts for variability among the profiles, errors in the retrieval, and uncertainties in the composition of the cloud. The presence of water ice substantially increases infrared cooling rates, due to its higher absorption cross section near the thermal emission peak. These snowfall percentages are generally consistent with GCM results by Forget et al. (1998). The MCS cloud opacity profiles and associated cooling rates suggest the majority of precipitation occurs within one ~7-km scale height of the surface, where optically thick clouds are perhaps most likely to occur based on the higher pressures and orographic effects (cf. Section 4 and Colaprete et al., 2008).

Advection of sensible heat into the polar atmosphere may offset radiative cooling, as described in Eq. (1). While the magnitude of Q_{Horz} may be highly variable in time and space, Pollack et al. (1990) modeled an average net flux of ~2 W m^{-2} into the polar night from lower latitudes based on the results of a Mars GCM, in agreement with earlier heat budget studies (Paige and Ingersoll, 1985). This is comparable in magnitude to the net radiative cooling

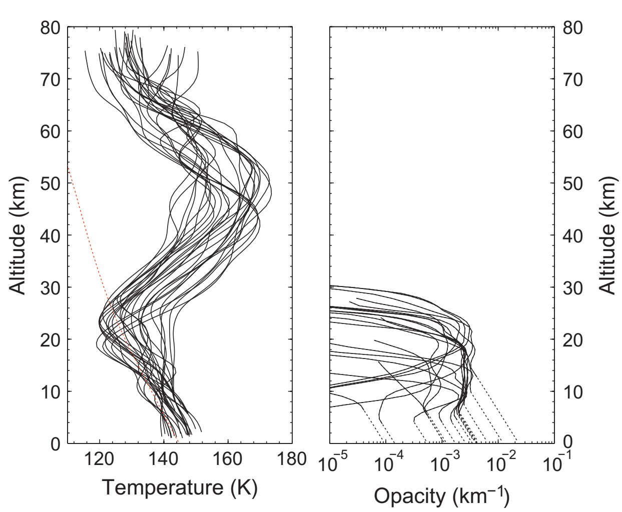

Fig. 2. Retrieved atmospheric profiles of temperature (left panel) and visible-wavelength CO_2 ice opacity (right) used in cooling rate calculations, corresponding to "orbit 2" in Fig. 1. The dotted red line indicates the CO_2 condensation profile. The majority of the temperature profiles are within a few degrees of the local frost point below ~30 km altitude, consistent with the locations of the retrieved CO_2 clouds. In some cases aerosol retrievals were unreliable in the lowermost layers (e.g. clouds were optically thick along the line of sight), in which case the dotted lines indicate extrapolation to the surface based on the assumption of a well-mixed atmosphere. (For interpretation of the references to colour in this figure legend, the reader is referred to the web version of this article.)

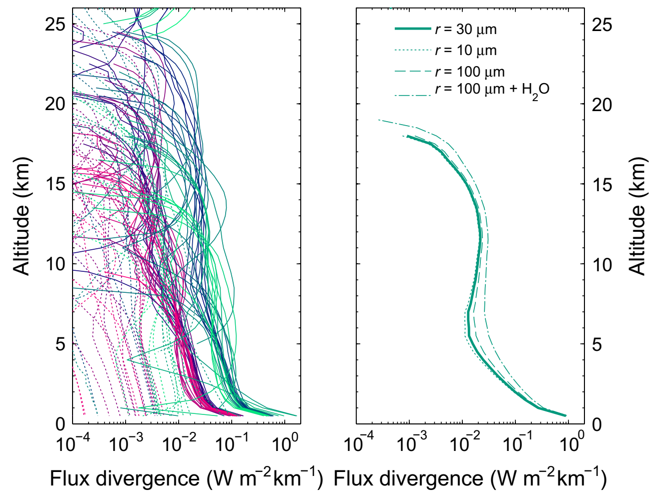

Fig. 3. Radiative flux divergence profiles for aerosol thermal emission (dotted lines at left) and gaseous thermal emission (solid lines) calculated from the atmospheric profiles of Fig. 1, assuming a surface infrared emissivity of 0.7 typical of the location and season. Profiles at left assume a CO_2 ice effective radius r_{eff} = 30 μm, whereas the right panel shows the effects of different grain sizes and the addition of water ice (0.1% mixing ratio of 10 μm grains) on an individual profile. Colors correspond to the locations shown in Fig. 1.

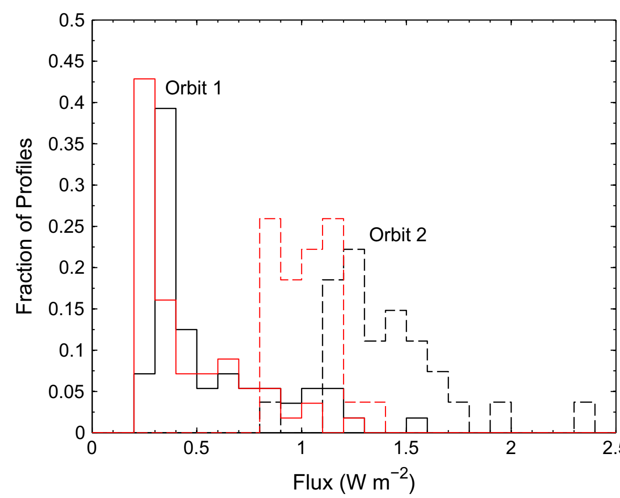

Fig. 4. Histograms of integrated atmospheric thermal emission show the distributions of values for two different MRO orbits on June 24, 2008 UTC (see Fig. 1). Red lines indicate fluxes calculated assuming a surface broadband infrared emissivity of 1.0, whereas the black lines indicate the more realistic value of 0.7.

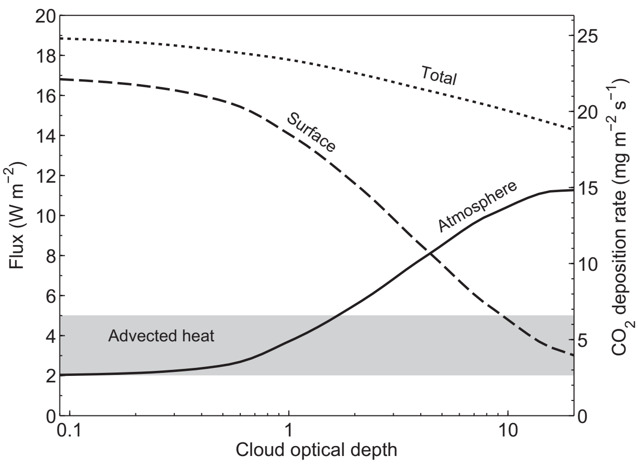

Fig. 5. Increase of atmospheric net radiative flux with increasing optical depth, for a CO_2 ice cloud with effective grain radius 100 μm, mixed with 0.1% water ice grains. Direct surface deposition (dashed line) decreases with increasing optical depth due to the blanketing effect caused by thermal infrared radiation scattered by the aerosols. The shaded box marks the modeled range in flux of heat advection into the polar regions from lower latitudes during polar winter (Pollack et al., 1990). Once the net infrared flux of the atmosphere rises above the advection flux, additional atmospheric condensation will occur, constituting a positive feedback loop on cloud formation.

within the atmosphere, suggesting that most of the atmosphere typically remains near saturation during polar night, consistent with temperature profiles retrieved by MCS in cloud-free regions (Fig. 2). In order to form the observed vertically-contiguous clouds, however, the net advection heat flux into the polar troposphere must have fallen at least briefly below the clear sky value of ~1 W m^{-2} (Table 1). On the other hand, the radiative cooling rates are not likely to ever be quite as low as the "clear sky" case, due to the presence of dust and water ice particles. In that case, radiative fluxes may always exceed the advection heat flux. For instance, Wood (1999) found that a cloudy atmosphere with dust visible optical depth $\tau_{dust} = 1.0$ experiences a net radiative flux of 6.2 W m^{-2}, in which case CO_2 ice precipitation would occur even if the advection flux is near the ~5 W m^{-2} estimate by Pollack et al. (1990) for such dusty conditions. A similar situation is most likely to occur in the dusty northern hemisphere during winter, especially after a large dust storm similar to that of MY28 (Kass et al., 2007). In contrast, dust optical depths this high have not been observed by MCS in the south polar winter, consistent with earlier observations (Pearl et al., 2001).

When carbon dioxide begins to condense in the atmosphere, the resulting cloud promotes further cooling. Because CO_2 ice retrievals are uncertain for optically thick clouds, we calculated cooling rates for a range of total optical depth. Fig. 5 shows that atmospheric infrared cooling rates increase rapidly with increasing optical depth, becoming the dominant heat balance term for $\tau_{vis} > 2$. This result suggests an interesting feedback phenomenon that may occur in the martian polar winter:

Table 1
Atmospheric radiative fluxes during south polar winter.[a]

Surface emissivity	Column-integrated radiative flux divergence (W m^{-2})			
	Clear	CO_2 30 μm	CO_2 100 μm	$CO_2 + H_2O$
1.0	0.7–1.2	0.8–1.3	0.8–1.5	0.8–2.0
0.7	0.7–2.0	0.8–2.3	0.9–2.5	1.1–2.9

[a] Opacity profiles used in calculating fluxes assume the given aerosol composition and the profiles retrieved at locations shown in Fig. 1.

1. The atmosphere cools to saturation when the radiative flux divergence plus dynamical cooling exceeds advection heating (aided by an influx of dust or water ice particles).
2. Carbon dioxide ice grains form on condensation nuclei, increasing the optical depth in the column.
3. Infrared cooling rates within the atmosphere increase due to higher optical depth and lower surface emissivity (due to snow grains), feeding back to step 2.

This process is illustrated in Fig. 6. The positive feedback between cloud formation and cooling can be halted or reversed when (1) the loss rate of particles due to precipitation at the surface exceeds their rate of formation in the atmosphere, (2) the influx of warmer gas molecules is enhanced due to decreasing CO_2 pressure in the column, and/or (3) atmospheric deposition becomes limited by the availability of condensation nuclei. In fact, a steady-state scenario could result where these negative feedbacks come to equilibrium with radiative cooling (Wood, 1999). The persistent nature of the clouds observed by MCS poleward of 80°S (Hayne et al., 2012) is consistent with such a model. The clearer atmosphere spanning latitudes 70–80°S (the "polar annulus", see Hayne et al., 2012) may be due to higher mean advection heating that is only occasionally overcome by radiative cooling. In addition, adiabatic cooling due to winds directed upslope is a potentially significant effect in initiating local snowstorms (Forget et al., 1998; Colaprete and Toon, 2002; Cornwall and Titus, 2009), which we discuss in the next section.

4. Adiabatic cooling

When the polar winter atmosphere is sub-saturated, topography may cause air directed upslope to cool rapidly by adiabatic expansion until CO_2 begins to condense. This orographic effect is expected to be more common in the southern hemisphere, where topographic relief is much greater than in the north (Smith et al., 2001). Of course, orographic waves also promote heating on lee slopes, such that their net effect on the polar winter heat balance may be negligible, while still initiating local snowstorms (see Fig. 5).

Winds in the south polar winter are typically of order 10 m s^{-1} and large scale flow is sub-cyclonic (McConnochie et al., 2003), such that west–northwest facing slopes are expected to cause the

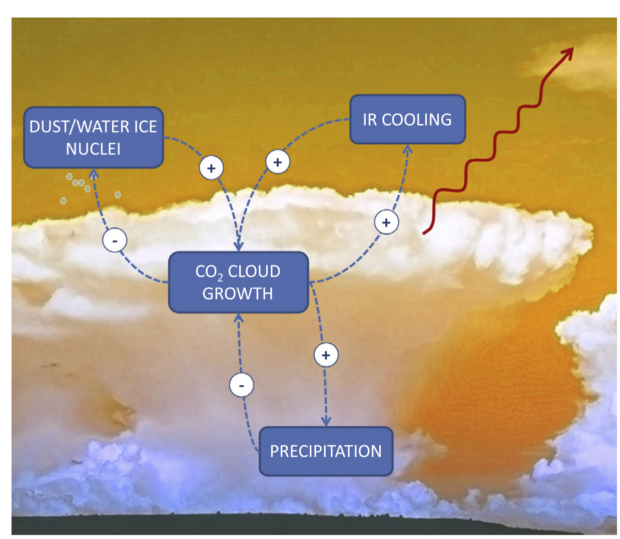

Fig. 6. A schematic representation of the feedbacks involved in forming CO_2 snow clouds on Mars. Positive and negative feedbacks are indicated by the circles on each arrow.

largest updrafts. To estimate the magnitude of adiabatic cooling from this effect, we calculated 400-km baseline slopes from MOLA topography, comparable to the scale of the largest clouds observed by MCS. The largest slopes are ~0.1–1.0% on this length scale, such that the upward wind component is $w \sim 0.01$–$0.1\ \mathrm{m\,s^{-1}}$. Adiabatic cooling occurs at a rate

$$\left[\frac{dT}{dt}\right]_{adv} = -w\left(\frac{g}{c_p} + \frac{dT_e}{dz}\right), \tag{5}$$

where T_e is the environment temperature. For a slightly sub-saturated environment temperature profile (Fig. 2), $dT_e/dz \sim 1\ \mathrm{K\,km^{-1}}$, and the dry adiabatic lapse rate $g/c_p \sim 5\ \mathrm{K\,km^{-1}}$, such that adiabatic cooling rates for 400-km south polar slopes are up to $\sim 10^{-4}\ \mathrm{K\,s^{-1}}$. By comparison, radiative cooling rates below 30 km are $\sim 10^{-5}$–$10^{-4}\ \mathrm{K\,s^{-1}}$ for the cloudy profiles considered above. Assuming the average advection heat flux of $\sim 2\ \mathrm{W\,m^{-2}}$ from the model of Pollack et al. (1990) is spread evenly from the surface to 80 km altitude, the associated heating rate below 30 km is also $\sim 10^{-5}$–$10^{-4}\ \mathrm{K\,s^{-1}}$. However, MCS temperature retrievals suggest a substantial portion of this energy may go into subsidence heating of the middle atmosphere (McCleese and et al., 2008), in which case the advection heating rates in the lower atmosphere may be $\ll 10^{-5}\ \mathrm{K\,s^{-1}}$. Furthermore, zonal asymmetries in meridonal heat transport may be very large, primarily due to the influence of Hellas basin, which sets up a strong wavenumber-1 pattern in the circumpolar jet. In any case, it is clear from their relative magnitudes that the combined adiabatic and infrared cooling rates above the steepest west-facing slopes are likely to periodically exceed heating due to advection and spur snowfall. The more extreme topography of the southern hemisphere is also likely to be more favorable to orographic cloud formation than the smoother northern plains, where radiative cooling may dominate the heat balance.

5. Sedimentation rates for the observed clouds

In the previous sections, we showed that the cloud profiles observed by MCS near the south polar residual cap are consistent with significant amounts of deposition occurring within the atmosphere, the majority likely within one scale height (~7 km) of the surface. In this section, we calculate sedimentation rates for the observed clouds, which provide an independent estimate of the fraction of carbon dioxide deposition occurring in the atmosphere. To begin with, we consider gravitational settling only, and then develop a diffusion model including effects of turbulence.

5.1. Gravitational settling

Normal optical depth is related to the extinction efficiency and number density by $\tau(z_1, z_2) = \int_{z_1}^{z_2} nQ_{ext}\alpha dz$, where α is the physical cross section of the cloud particles, and Q_{ext} is their extinction efficiency at the wavelength of the observation. The number density at an altitude z is then

$$n(z) = \frac{\partial \tau}{\partial z}/Q_{ext}\alpha. \tag{6}$$

Cloud number density profiles can be used to estimate the sedimentation rate with some knowledge of their particle size distribution and temperature profile. It is instructive to begin by considering the motion of particles under the influence of gravity without atmospheric turbulence; the more realistic case will be considered later. The mass flux due to pure gravitational settling is $dm/dt = nw_0\bar{m}_p$, where $\bar{m}_p$ is the average particle mass, and w_0 is the gravitational settling velocity, given by the Stokes–Cunningham law for spherical particles (Ryan, 1964; Rossow, 1978):

$$w_0(z) = (2\rho_s g r^2/9\eta)(1 + \lambda/r). \tag{7}$$

Here ρ_s is the solid density of the aerosol particle of radius r, $\eta \approx 8.5 \times 10^{-6}$ Pa s is the molecular viscosity of the atmosphere at 150 K (Catalfamo et al., 2009), and g is the gravitational acceleration. The molecular mean free path is

$$\lambda = \frac{k_B T}{\sqrt{2}\pi d^2 p}, \tag{8}$$

where $d \approx 3$ Å is the molecular diameter of CO_2, and k_B is Boltzmann's constant. At an altitude of 10 km, settling velocities for 10 μm, 30 μm, and 100 μm particles of CO_2 are approximately 0.17, 0.8, and 5.6 $\mathrm{m\,s^{-1}}$ respectively. While the motion of a snow particle through the atmosphere may be complex, it is nonetheless useful to define a characteristic gravitational settling time (Conrath, 1975):

$$t_s(z) = H/w_0(z), \tag{9}$$

where H is the pressure scale height, roughly 7 km in the polar winter. Settling times for several different altitudes are plotted in Fig. 7.

Since settling velocities decrease with increasing pressure, if particles do not grow appreciably as they fall, they will tend to accumulate in the lower part of the atmosphere. Over the poles, where orbit tracks converge, MCS observes essentially the same region on successive orbits. Fig. 7 also suggests (again, neglecting turbulence) that particles larger than ~100 μm cannot remain in the atmosphere long enough to be observed on more than one ~2-h orbit of the MRO spacecraft, and therefore must be continuously resupplied. The cloud opacity in the lowest scale height in the south polar region is typically ~0.001–0.01 $\mathrm{km^{-1}}$ (Fig. 2), giving a gravitational settling flux of $\sim 10^{-9}$–$10^{-5}\ \mathrm{kg\,m^{-2}\,s^{-1}}$ for grain radii 10–100 μm. The upper end of this range is comparable to the total surface-atmosphere deposition rate of ~ 2–$4 \times 10^{-5}\ \mathrm{kg\,m^{-2}}$ - $\mathrm{s^{-1}}$, and is consistent with the highest snowfall rates encountered in the simulations of Colaprete et al. (2008). These results suggest snowfall from the observed south polar clouds may contribute significantly to the total accumulation at the surface, consistent with the results of the cooling rate calculations presented in Section 3.

5.2. Turbulent snowfall model

The simplified model for the sedimentation of cloud particles presented above provides some insight into the process, but neglects the potentially important effects of turbulence encountered

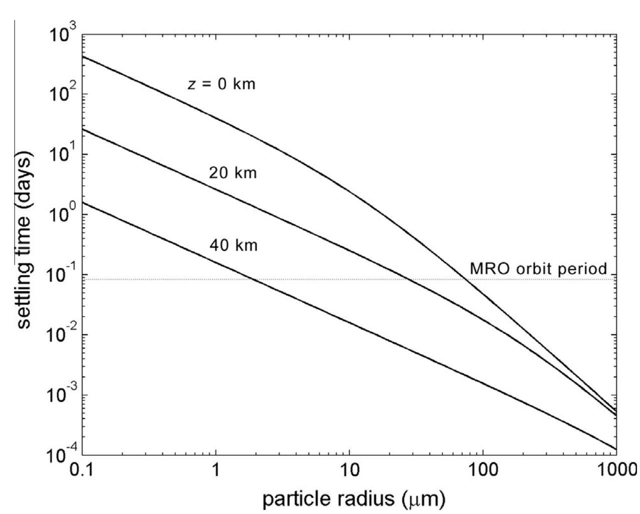

Fig. 7. Gravitational settling times for a range of CO_2 ice particle sizes, at three different altitudes. The approximate period of the Mars Reconnaissance Orbiter is shown as the dotted line, below which clouds may be expected to precipitate to the surface before multiple observations can be taken.

by falling snow particles in the martian atmosphere. Furthermore, gravitational settling cannot accurately capture the time evolution of the cloud profile, which may provide insight into the MCS observations. In the more general case, vertical diffusion of a snow cloud with number density profile $n(z)$ can be represented by (cf. Conrath, 1975):

$$\frac{\partial n}{\partial t} = \frac{\partial}{\partial z}\left(K\frac{\partial n}{\partial z} + w_0 n\right), \tag{10}$$

where the first term on the right-hand side accounts for flow due to vertical mixing, and the second term represents gravitational settling. The eddy diffusion coefficient of the martian atmosphere K is not well constrained (Izakov, 2007), though solar occultation measurements (Korablev et al., 1993; Chassefiere et al., 1992) and photochemical models (von Zahn and Hunten, 1982) give values consistently in the range 10^2–10^3 $m^2\,s^{-1}$ in the lower atmosphere, though the polar winter atmosphere may be more statically stable than in the tropics (Colaprete et al., 2008). Lacking a better constraint, we explored the snowfall behavior for this full range, and find that the results are relatively insensitive to this parameter. While K may vary with height in the atmosphere, this variation is unknown and is probably less than a factor of ~5 for the region in which cloud particles are found (see Fig. 2 of Bittner and Fricke, 1987). Therefore, we make the simplifying assumption $K(z)$ = constant, such that the expanded mass diffusion equation becomes

$$\frac{\partial n}{\partial t} = K\frac{\partial^2 n}{\partial z^2} + w_0\frac{\partial n}{\partial z} + n\frac{\partial w_0}{\partial z}. \tag{11}$$

In addition to the initial number density profile $n(z)$, boundary conditions to (11) must be supplied. At the top of the atmosphere, it is safely assumed that $n \to 0$. Calder (1961) discussed the lower boundary condition in the context of terrestrial precipitation, concluding that the downward flux at the surface should be proportional to the local number density. The simplest choice for the constant of proportionality is the gravitational settling velocity w_0, an approximation that holds for large particles (Conrath, 1975; Lick, 1982). In this case, the second-order diffusive term in (11) vanishes

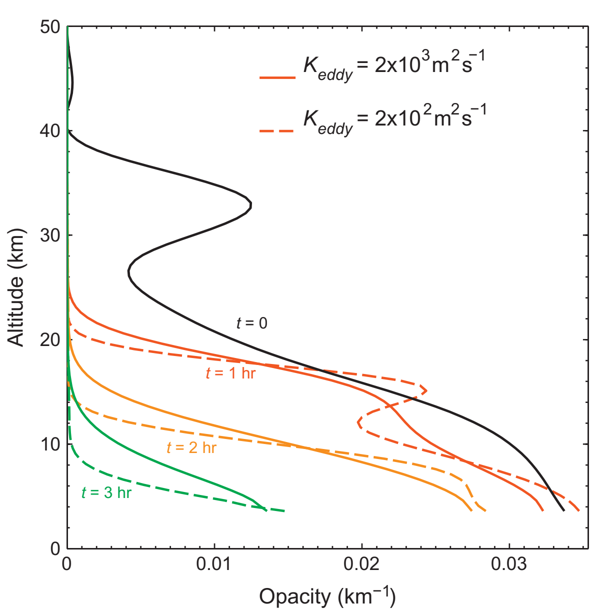

Fig. 8. Evolution of a falling snow cloud: opacity profiles for a CO_2 cloud with effective particle radius 100 µm. Results for two different values of the eddy viscosity K are shown: 2.0×10^3 (solid lines) and 2.0×10^2 (dashed lines). Order of magnitude variations in K alter the shape of the profile, but have little effect on the overall decay of the cloud.

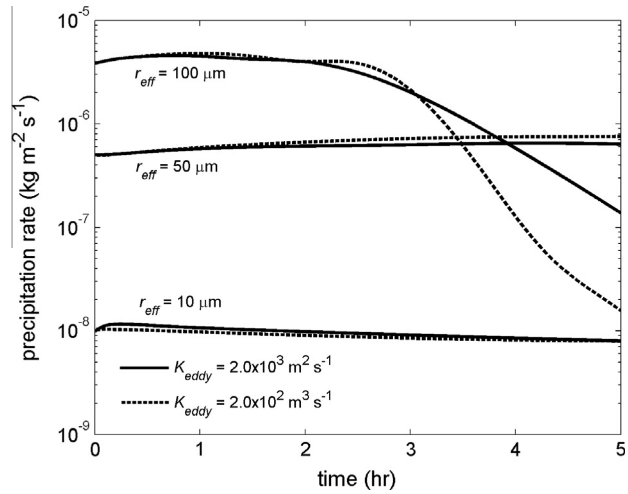

Fig. 9. Modeled precipitation rates versus time for the cloud with visible opacity ~0.5 observed by MCS over the south polar residual cap. The three different particle sizes result in very different peak snowfall rates and cloud dissipation time scales. Solid lines assume an eddy viscosity $K = 2 \times 10^3\,m^2\,s^{-1}$, and dashed lines $2 \times 10^2\,m^2\,s^{-1}$.

at the surface, i.e. $\partial^2 n/\partial z^2 = 0$ and the flux boundary condition becomes

$$F^{\downarrow}_{snow} \approx (w_0 n)_{z=0}. \tag{12}$$

We solved (10) numerically, subject to the two boundary conditions, the initial number density profiles retrieved for a typical south polar CO_2 cloud, and a range of particle sizes. The one-dimensional mass diffusion model employs a standard finite difference scheme, typically with ~200 layers, each 500 m thick. The atmosphere is assumed to be isothermal at 140 K, with a pressure scale height of 7.1 km. Fig. 8 shows the time evolution of an observed south polar cloud for an effective grain radius of 100 µm. The profile shows gradual smoothing due to vertical mixing, while snowfall at the surface reduces the total cloud optical depth just as the relative abundance of particles in the lowest levels increases.

Precipitation rates for particle radii of 10, 50 and 100 µm are shown in Fig. 9 for the observed cloud. Snowfall gradually decays as the cloud thins, which occurs most rapidly for large particles. Larger particles also generate much higher initial precipitation rates, thinning the cloud on a time scale of just a few hours, while fine-grained clouds may persist for days. Initial precipitation rates predicted by the model for 10, 50 and 100 µm particles are $\sim 1 \times 10^{-8}$, 5×10^{-7}, and 3×10^{-6} kg $m^{-2}\,s^{-1}$, respectively, corresponding to ~0.05–15% of the total deposition rate within the surface-atmosphere column. The total quantity of CO_2 ice deposited by snowfall depends on the particle size, cloud optical depth, and the rate at which clouds are re-formed. As discussed above, particle sizes are likely to be in the range 30–100 µm, which is consistent with the derived precipitation rates considering that MCS observed clouds dissipating on the ~2-h time scale of the MRO orbit (Hayne et al., 2012). Because the $\tau_{vis} \sim 0.5$ cloud considered here is typical of those commonly observed poleward of 80°S during mid-late winter, the results of this section lend further support to the hypothesis that a substantial portion of the seasonal cap in this region is deposited by snowfall originating in the lowermost pressure scale height. In the region 60–80°S where thick clouds are more sporadic, snowfall may be less significant, or confined to lower altitudes. Finally, the results of this section suggest that snowfall in the northern hemisphere may be quite different, because higher surface pressures will tend to increase fall times

Table 2
CO_2 15-μm equivalent width matrix parameter values.[a]

Parameter	$\bar{\mu}$	d_0	T_0	q_d	q_f	f_0	a	b
Value	0.488	54.4	300 K	0.879	−0.256	0.153	0.323	0.566

[a] Pollack et al. (1981).

and keep particles in suspension, while atmospheric radiative cooling rates are also higher; therefore snow grains might be expected to grow larger than in the south.

6. Conclusions

In this paper, we presented atmospheric CO_2 deposition and particle sedimentation rates based on polar winter atmospheric profiles observed by the Mars Climate Sounder. The results suggest a substantial fraction of total CO_2 deposition during the winter season occurs as snowfall, for a reasonable range of snow particle sizes and compositions. Our conclusions can be summarized as follows:

1. Net infrared emission by the cloudy south polar winter atmosphere is $\sim$2.0 W m^{-2} for the observed clouds with $\tau_{vis} \sim 0.1$, allowing up to $\sim$20% of total deposition to occur as snowfall originating below $\sim$30 km altitude. Substantially greater atmospheric deposition (a majority of the total) can occur if the clouds become optically thick with $\tau_{vis} > 2$.
2. Dynamical (i.e. adiabatic) cooling due to orographic lifting on a $\sim$400 km horizontal scale can generate cooling rates up to an order of magnitude larger than radiative cooling rates for the model atmosphere with $\tau_{vis} < 0.5$. However, radiative cooling rates within thicker clouds can meet or exceed the adiabatic rate on this spatial scale.
3. Radiative and dynamical cooling can be offset by horizontally transported heat from latitudes outside the polar night. While this quantity is poorly constrained, heat balance studies (Paige and Ingersoll, 1985) and GCMs (Pollack et al., 1990) suggest a mean wintertime influx of $\sim$2 W m^{-2}. Because this is comparable to the net radiative flux for the observed clouds, most of the polar winter atmosphere is likely to be sub-saturated until condensation is triggered by: (1) an influx of dust or water ice (providing condensation nuclei and increasing cooling rates), (2) adiabatic cooling by vertical motion, and/or (3) a temporary decrease in sensible heat flux, perhaps locally.
4. Once CO_2 begins condensing in the atmosphere, a positive feedback on radiative cooling may occur, which results in runaway growth of the snow cloud. A second positive feedback is provided by the reduction in surface emissivity during a snowstorm, which causes atmospheric cooling. Equilibrium may be achieved when precipitation at the base of the cloud balances condensation of new ice grains. Similar steady-state scenarios were modeled in detail by Wood (1999).
5. Snowfall rates derived from infrared fluxes observed by MCS are generally consistent with snowfall rates calculated from sedimentation velocities for 50–100 μm CO_2 ice particles. Estimating the total seasonal snowfall with this method depends on knowledge of the typical grain size, cloud optical depth and frequency. Future work will include better constraining these quantities using the rich MCS dataset, though observed cloud lifetimes of less than several hours suggest a lower limit of $\sim$50 μm on the typical cloud grain size (Fig. 9).

Together, these results suggest that carbon dioxide snowfall makes a substantial contribution to the martian south polar seasonal ice caps, especially in the cloudiest regions poleward of 80°S. Radiative cooling rates and snow sedimentation models presented here provide an upper bound of $\sim$20% by mass of CO_2 deposited as snow during the observation period at $L_s = 85°$. A lower limit on snowfall rates is difficult to establish, because this depends on the effective grain size of the cloud particles, which is relatively poorly constrained. However, considering the very short lifetimes of some clouds, we established a lower limit of $\sim$50 μm on the grain size, which yields a lower bound on the precipitation of $\sim$7% by mass of CO_2 deposited as snowfall. This effective grain size is consistent with the spectroscopic data presented by Hayne et al. (2012). Outside the extreme polar regions, clouds are more sporadic and lower-lying, such that it is difficult to retrieve their optical depths from the MCS measurements (Hayne et al., 2012). However, wintertime cloud activity was observed to increase toward the pole (in both hemispheres), suggesting a variable role for snowfall at different latitudes. In fact, southern hemisphere CO_2 cloud activity is most intense over the south residual cap, which may therefore experience more abundant snowfall relative to the rest of the seasonal cap. If the granularity of these deposits can be maintained until springtime, this observation might partly explain the enhanced albedo of the seasonal deposits on top of the residual cap (Colaprete et al., 2005; Langevin et al., 2007). Furthermore, because snow deposits are likely to be less dense than those condensing directly at the surface, they could play a critical role in determining the thickness of the seasonal deposits.

Acknowledgments

We gratefully acknowledge fruitful discussions with J. Shirley, D. Kass, J.T. Schofield, D. McCleese, and A. Colaprete. The paper also benefited from the criticism of two anonymous reviewers. Part of this research was performed at the Jet Propulsion Laboratory, California Institute of Technology, under contract with the National Aeronautics and Space Administration.

Appendix A. Infrared atmospheric cooling rates

Radiative cooling rates are determined by the local flux divergence:

$$\frac{dT}{dt} = \frac{g}{c_p}\frac{dF}{dp}, \tag{13}$$

where g is the acceleration of gravity, c_p is the temperature-dependent specific heat of the atmosphere, and p is the local gas pressure. In an N-layer model, the radiative flux divergence at layer i is

$$\frac{dF}{dp} \approx \frac{\Delta F_i}{\Delta p_i} = \frac{1}{\Delta p_i}\left[\left(F_i^{\uparrow} - F_i^{\downarrow}\right) - \left(F_{i+1}^{\uparrow} - F_{i+1}^{\downarrow}\right)\right], \tag{14}$$

where Δp_i is the pressure difference between layers i and $i + 1$, and $F_i^{\uparrow}$ and $F_i^{\downarrow}$ are the diffuse upward and downward infrared fluxes at layer i. It is important to use sufficiently thin layers (typically <1 km) such that the approximation in (14) holds. During polar night, insolation is zero, so that diabatic heating or cooling occur only through the transfer of infrared radiation. On Mars, the two primary sources of infrared emission and absorption are CO_2 gas and aerosols (CO_2 ice, dust and water ice). Cooling rates due to these two sources are treated in each of the following sections.

A.1. Aerosol cooling rates

In the δ-Eddington approximation (Joseph et al., 1976; Hayne et al., 2012), the monochromatic upward and downward fluxes are

$$F_{\nu}^{\downarrow\uparrow}(\tau) = 2\pi\int_0^{\pm 1}(I_0 + \mu I_1)\mu d\mu = \pi[I_0(\nu,\tau) \pm \frac{2}{3}I_1(\nu,\tau)], \tag{15}$$

so that from Eq. (3) the net monochromatic flux between levels τ_i and τ_{i+1} is

$$\Delta F_\nu(\tau_i) = \frac{4\pi}{3}[I_1(\nu,\tau_{i+1}) - I_1(\nu,\tau_i)]. \tag{16}$$

The flux divergence between each pair of atmospheric levels can be calculated by integrating (16) over all frequencies, given the calculated values of $I_1(\nu,\tau)$ and the pressure at each level, and subject to the following boundary conditions on the spectral fluxes at the top and bottom of the atmosphere:

$$\begin{aligned} F^{\downarrow}_{top} &= 0 \\ F^{\uparrow}_{bot} &= (1-\varepsilon_\nu)F^{\downarrow}_{bot} + \pi\varepsilon_\nu B_\nu(T_s). \end{aligned} \tag{17}$$

Here, ε_ν is the emissivity of the surface at the given frequency, and $B_\nu(T_s)$ is the blackbody radiance at the surface kinetic temperature. In practice, these boundary conditions and the net spectral fluxes (15) are readily calculated as a byproduct of the δ-Eddington forward model of Hayne et al. (2012), and are then integrated across an appropriate range of wavelengths (typically 10–50 μm) to find the total net flux at each level in the atmosphere for a given aerosol opacity profile.

A.2. Cooling within the gaseous CO_2 15 μm band

During the martian polar winter, thermal emission by the ~150 K atmosphere occurs almost entirely via transitions associated with the 15 μm (667 cm^{-1}) bending fundamental of gaseous CO_2. Exact line-by-line methods for calculating infrared opacities within this band are computationally expensive, and much more efficient approximate methods are often suitably accurate for flux calculations used in climate studies (Crisp et al., 1986). In an N-layer atmosphere the upward and downward fluxes at level i can be represented by sums over the equivalent widths of the other model layers:

$$\begin{aligned} F^{\downarrow}_{15}(i) &= 2\pi\sum_{j=2}^{i} B_{15}(T_{j-1})[E_{i,j-1} - E_{i,j}] \\ F^{\uparrow}_{15}(i) &= 2\pi B_{15}(T_s)[\Delta\nu_{15}/2 - E_{i,N+1}] + 2\pi\sum_{j=i}^{N} B_{15}(T_{j+1})[E_{i,j+1} - E_{i,j}], \end{aligned} \tag{18}$$

where $B_{15}(T)$ is the blackbody radiance at the center of the 15 μm band, T_s is the surface temperature, and $\Delta\nu_{15}$ is a "nominal width" of the band, the choice of which has no effect on the net cooling rate in each layer. The upper and lower boundary conditions are

$$\begin{aligned} F^{\downarrow}_{15}(1) &= 0 \\ F^{\uparrow}_{15}(N+1) &= \pi B_{15}(T_s)\Delta\nu_{15}. \end{aligned} \tag{19}$$

The matrix $E_{i,j}$ specifies the flux equivalent widths of each layer with respect to every other layer, which can be calculated by a variety of techniques. An empirical model for the 15 μm CO_2 band was developed by Pollack et al. (1981) by fitting a function of the following form to laboratory data on the infrared transmissivity of CO_2 gas under Mars-like conditions:

$$E_{i,j} = \bar{\mu} d_0 \left(\frac{\overline{T}_{i,j}}{T_0}\right)^{q_d} \ln\left[1 + f_0\left(\frac{\overline{T}_{i,j}}{T_0}\right)^{q_f} w^b \bar{p}^a\right], \tag{20}$$

where $\overline{T}_{i,j}$ is the pressure-weighted average temperature between levels i and j, $\bar{p}$ is the average pressure (in millibars) over this interval, and $w = 1305.5\Delta p$ is the absorber path length (atmos-cm) for the pressure difference Δp (in millibars). Values for the other parameters in (20) are given in Table 2. Inserting the equivalent width matrix (20) into (18) gives the upward and downward fluxes needed to estimate the flux divergence profile from (14). A similar method was successfully applied by Paige and Ingersoll (1985) for the calculation of Mars polar equilibrium temperature profiles, and also by Wood (1999) as a component of a steady-state snowfall model.

References

Bittner, H., Fricke, K.H., 1987. Dayside temperatures of the martian upper atmosphere. J. Geophys. Res. 92, 12045–12055.

Calder, K.L., 1961. Atmospheric diffusion of particulate material considered as a boundary value problem. J. Meteorol. 18, 413–416.

Catalfamo, C., Bruno, D., Colonna, G., Laricchiuta, A., Capitelli, M., 2009. High temperature Mars atmosphere. Part II: Transport properties. Eur. Phys. J. 54, 613–621.

Chassefiere, E., Blamont, J.E., Krasnopolsky, V.A., Korablev, O.I., Atreya, S.K., West, R.A., 1992. Vertical structure and size distributions of martian aerosols from solar occultation measurements. Icarus 97, 46–69.

Clancy, R.T. et al., 2000. An intercomparison of ground-based millimeter, MGS TES, and Viking atmospheric temperature measurements: Seasonal and interannual variability of temperatures and dust loading in the global Mars atmosphere. J. Geophys. Res. 105, 9553–9571. http://dx.doi.org/10.1029/1999JE001089.

Clark, R.N., Fanale, F.P., Zent, A.P., 1983. Frost grain size metamorphism – Implications for remote sensing of planetary surfaces. Icarus 56, 233–245.

Colaprete, A., Toon, O.B., 2002. Carbon dioxide snow storms during the polar night on Mars. J. Geophys. Res. 107 (E7), 50501–50516. http://dx.doi.org/10.1029/2001JE001758.

Colaprete, A., Haberle, R.M., Toon, O.B., 2003. Formation of convective carbon dioxide clouds near the south pole of Mars. J. Geophys. Res. 108 (E7), 5081. http://dx.doi.org/10.1029/2003JE002053.

Colaprete, A., Barnes, J.R., Haberle, R.M., Hollingsworth, J.L., Kieffer, H.H., Titus, T.N., 2005. Albedo of the south pole on Mars determined by topographic forcing of atmosphere dynamics. Nature 435, 184–188.

Colaprete, A., Barnes, J.R., Haberle, R.M., Montmessin, F., 2008. CO_2 clouds, CAPE and convection on Mars: Observations and general circulation modeling. Planet. Space Sci. 56, 150–180.

Conrath, B.J., 1975. Thermal structure of the martian atmosphere during the dissipation of the dust storm of 1971. Icarus 24, 36–46.

Cornwall, C., Titus, T.N., 2009. Spatial and temporal distributions of martian north polar cold spots before, during, and after the global dust storm of 2001. J. Geophys. Res. 114, E02003.

Crisp, D., Fels, S.B., Schwarzkopf, M.D., 1986. Approximate methods for finding CO_2 15-micron band transmission in planetary atmospheres. J. Geophys. Res. 91, 11851–11866.

Eluszkiewicz, J., 1993. On the microphysical state of the martian seasonal caps. Icarus 103, 43–48.

Eluszkiewicz, J., Moncet, J.-L., Titus, T.N., Hansen, G.B., 2005. A microphysically-based approach to modeling emissivity and albedo of the martian seasonal caps. Icarus 174, 524–534.

Forget, F., Hourdin, F., Talagrand, O., 1998. CO_2 snowfall on Mars: Simulation with a general circulation model. Icarus 131, 302–316.

Gierasch, P.J., Goody, R.M., 1968. A study of the thermal and dynamical structure of the martian lower atmosphere. Planet. Space Sci. 16, 615–646.

Hansen, G.B., 1999. Control of the radiative behavior of the martian polar caps by surface CO_2 ice: Evidence from Mars Global Surveyor measurements. J. Geophys. Res. 104, 16471–16486.

Hayne, P.O., Paige, D.A., Schofield, J.T., Kass, D.M., Kleinbohl, A., Heavens, N.G., McCleese, D.J., 2012. Carbon dioxide snow clouds on Mars: South polar winter observations by the Mars Climate Sounder. J. Geophys. Res. 117, E08014. http://dx.doi.org/10.1029/2011JE004040.

Hu, R., Cahoy, K., Zuber, M.T., 2012. Mars atmospheric CO2 condensation above the north and south poles as revealed by radio occultation, climate sounder, and laser ranging observations. J. Geophys. Res. 117, E07002. http://dx.doi.org/10.1029/2012JE004087.

Ivanov, A.B., Muhleman, D.O., 2001. Cloud reflection observations: Results from the Mars orbiter laser altimeter. Icarus 154, 190–206.

Izakov, M.N., 2007. Turbulence in the free atmospheres of Earth, Mars, and Venus: A review. Solar Syst. Res. 41, 355–384.

Joseph, J.H., Wiscombe, W.J., Weinman, J.A., 1976. The delta-Eddington approximation for radiative flux transfer. J. Atmos. Sci. 33, 2452–2459.

Kass, D.M., McCleese, D., Schofield, T., Kleinboehl, A., Zurek, R., Bowles, N., 2007. MCS views of the 2007 global dust storm. Bull. Am. Astron. Soc. 39, 441.

Kleinböhl, A. et al., 2009. Mars Climate Sounder limb profile retrieval of atmospheric temperature, pressure, and dust and water ice opacity. J. Geophys. Res. 114, E10006. http://dx.doi.org/10.1029/2009JE003358.

Korablev, O.I., Krasnopolsky, V.A., Rodin, A.V., Chassefiere, E., 1993. Vertical structure of martian dust measured by solar infrared occultations from the PHOBOS spacecraft. Icarus 102, 76–87.

Kuroda, T., Medvedev, A.S., Kasaba, Y., Hartogh, P., 2013. Carbon dioxide ice clouds, snowfalls, and baroclinic waves in the northern winter polar atmosphere of Mars. Geophys. Res. Lett. 40, 1484–1488. http://dx.doi.org/10.1002/grl.50326.

Langevin, Y. et al., 2007. Observations of the south seasonal cap of Mars during recession in 2004–2006 by the OMEGA visible/near-infrared imaging spectrometer on board Mars Express. J. Geophys. Res. 112, E08S12. http://dx.doi.org/10.1029/2006JE002841.

Lick, W., 1982. The transport of contaminants in the great lakes. Annu. Rev. Earth Planet. Sci. 10, 327–353.
McCleese, D.J. et al., 2007. Mars Climate Sounder: An investigation of thermal and water vapor structure, dust and condensate distributions in the atmosphere, and energy balance of the polar regions. J. Geophys. Res. 112, E05S06. http://dx.doi.org/10.1029/2006JE002790.
McCleese, D.J. et al., 2008. Intense polar temperature inversion in the middle atmosphere on Mars. Nat. Geosci. 1, 745–749.
McConnochie, T.H., Conrath, B.J., Gierasch, P.J., Banfield, D., Smith, M.D., 2003. Observations of the Mars Polar Vortex. In: Sixth Int. Conf. Mars, July 20–25, 2003, Pasadena, California (abstract no. 3248).
Neumann, G.A., Smith, D.E., Zuber, M.T., 2003. Two Mars years of clouds detected by the Mars Orbiter Laser Altimeter. J. Geophys. Res. 108 (E4), 5023. http://dx.doi.org/10.1029/2002JE001849.
Paige, D.A., Ingersoll, A.P., 1985. Annual heat balance of martian polar caps – Viking observations. Science 228, 1160–1168.
Pearl, J.C., Smith, M.D., Conrath, B.J., Bandfield, J.L., Christensen, P.R., 2001. Observations of martian ice clouds by the Mars Global Surveyor Thermal Emission Spectrometer: The first martian year. J. Geophys. Res. 106, 12325–12338.
Pollack, J.B., Leovy, C.B., Greiman, P.W., Mintz, Y., 1981. A martian general circulation experiment with large topography. J. Atmos. Sci. 38, 3–29.
Pollack, J.B., Haberle, R.M., Schaeffer, J., Lee, H., 1990. Simulations of the general circulation of the martian atmosphere. I – Polar processes. J. Geophys. Res. 95, 1447–1473.
Rossow, W.B., 1978. Cloud microphysics – Analysis of the clouds of Earth, Venus, Mars, and Jupiter. Icarus 36, 1–50.
Ryan, J.A., 1964. Notes on the martian yellow clouds. J. Geophys. Res. 69, 3759–3770.
Smith, D.E. et al., 2001. Mars Orbiter Laser Altimeter: Experiment summary after the first year of global mapping of Mars. J. Geophys. Res. 106, 23689–23722.
Titus, T.N., Kieffer, H.H., Mullins, K.F., Christensen, P.R., 2001. TES premapping data: Slab ice and snow flurries in the martian north polar night. J. Geophys. Res. 106, 23181–23196.
von Zahn, U., Hunten, D.M., 1982. Aeronomy of Mars' Lower Atmosphere: Status and Prospects. Eur. Space Agency Spec. Publ., ESA-SP 185, pp. 37–46.
Wood, S.E., 1999. Nucleation and Growth of Carbon Dioxide Ice Crystals in the Martian Atmosphere. Ph.D. Thesis, University of California, Los Angeles, Source DAI-B 60/04, October 1999, 192 p. (p. 1653).